Construction and Building Materials 476 (2025) 141240

Contents lists available at ScienceDirect

Construction and Building Materials

journal homepage: www.elsevier.com/locate/conbuildmat

Ultra-high-performance alkali-activated concrete produced with desert sand incorporations

Ming Zhang [a,b], Pengfei Hu [c], Shangyu Sun [a], Jie Yao [d], Yubo Sun [e,*], Jing Zhong [a,*]

[a] *School of Civil Engineering, Harbin Institute of Technology, Harbin 150001, China*
[b] *China State Construction International Holdings Limited, 999077, Hong Kong*
[c] *School of Civil Engineering and Architecture, Wuhan Polytechnic University, Wuhan 430023, China*
[d] *China State Construction Hailong Technology Co., Ltd., Shenzhen 518000, China*
[e] *Department of Civil and Environmental Engineering, The Hong Kong Polytechnic University, 999077, Hong Kong*

ARTICLE INFO

Keywords:
Desert sand
Ultra-high-performance concrete
Alkali-activated materials
Microstructures
Reaction products

ABSTRACT

The global surge in construction has intensified demand for natural silica sand (SS), causing shortages due to unsustainable extraction. This study explores the potential of using desert sand (DS) as an alternative to SS in producing ultra-high-performance alkali-activated concrete (UHPAAC), emphasizing the interactions between aggregates and the binding matrix. DS demonstrated a smoother surface morphology, finer particles, and a narrower gradation compared to SS. Substituting SS with DS at varying volume ratios improved the concentration of several elements in the pore solution of fresh mixtures. Samples with 10 vol% DS achieved the highest compressive strength, about 20 % higher than the SS reference mix. However, higher DS content reduced mechanical performance. Investigations of reaction products and microstructural characteristics revealed changes in the binder phase, including a lower Ca/Si ratio and improved local elastic modulus when DS was incorporated. Additionally, the smaller grain sizes of DS created numerous interfaces with the binding matrix, resulting in a more porous microstructure and declined micromechanical properties in the interfacial transition zone (ITZ) compared to SS. Nevertheless, the strategic incorporation of DS as a partial replacement for SS enhances both compressive and flexural strength while simultaneously reducing the environmental impact of UHPAAC production.

1. Introduction

Concrete is a widely used material in the construction industry, with an estimated annual usage of 30 billion tons worldwide [1,2]. The demand for concrete products has been steadily increasing due to extensive building and infrastructure construction in emerging economies during the past decades. This has driven up the need for raw materials such as cementitious binder, sand, gravel, and additives. Approximately 46 % of all materials extracted from the earth are used in global concrete and mortar productions [3,4]. Natural silica sand (SS) is a common fine aggregate applied in cementitious composites, while high-quality deposits are unevenly distributed, leading to regional shortages and increased competition for resources. Countries with limited natural resources, such as Singapore and the United Arab Emirates, have faced persistent sand shortages, resulting in substantial expenditures on importing sand for large-scale projects [5,6]. The scarcity of SS has led to rising prices, impacting the overall cost of construction projects and potentially causing delays. In the meantime, over-exploitation of natural resources, especially SS, can lead to severe ecological and environmental issues, such as coastal erosion, sedimentation, riverbed degradation, and water table sinkage [7]. Many countries have implemented stricter environmental regulations and land-use policies, limiting the extraction of natural SS. To mitigate these negative impacts, replacing SS with other materials, such as desert sand (DS) substitution, is considered a promising alternative [8].

Deserts have encroached upon vast areas of land globally, and anthropogenic activities are accelerating desertification, further disrupting the natural ecosystem [9]. Extensive studies have revealed that DS is abundantly available on the earth up to 6 million km^3 [10]. Similar to SS, the dominant chemical component of DS is SiO_2, accounting for 55.61–82.66 % by mass, as determined from samples collected across various regions worldwide [11,12]. Though DS shares the same main

---

* Corresponding authors.
E-mail addresses: yubo.sun@polyu.edu.hk (Y. Sun), zhongjing@hit.edu.cn (J. Zhong).

https://doi.org/10.1016/j.conbuildmat.2025.141240
Received 21 January 2025; Received in revised form 1 April 2025; Accepted 6 April 2025

components with SS, it is inappropriate for direct massive usage in the construction sector. Above all, DS has a poor gradation with great uniformity compared to the natural SS, which is ascribed to the selective sorting of long-term wind blowing [13]. Moreover, most DS samples are characterized by a spherical particle coupled with relatively smooth and flat surface morphology, due to the intensive pitting process [14]. From the chemical perspective, DS is slightly basic, featuring an elevated pH value compared to that of SS [15]. Recent scholars have shown that when added in proportionate amounts, DS demonstrates great capability to replace either natural aggregates or cementitious binders in concrete mixes, offering potential benefits in workability, strength, and durability compared to those prepared with SS [16–18].

While these advancements in DS utilization present partial solutions for sustainable construction, they must be contextualized within the broader environmental challenges confronting the industry. In specific, rapid urbanization and industrialization have led to increased human activities in the civil and construction sectors, exacerbating environmental issues and accelerating global warming. Scrivener and Kirkpatrick emphasized that concrete and cement production has contributed over 8 % of global CO_2 emissions [19], primarily originating from the calcination of cement clinkers. With the advances of modern concrete technology, ultra-high-performance concrete (UHPC) was developed in the early 1990s to provide superior performances in particular in strength, ductility, and durability over conventional concrete mixtures [20,21]. UHPC has been widely applied in modern infrastructures, for instance, bridges, skyscrapers, evacuation platforms, and long-span structures [22]. However, UHPC has on the other hand elevated the Portland cement (PC) content to a new level (around 800–1100 kg/m^3) from the mix design perspective, which further amplifies the environmental impact of unit volume concrete [23,24]. To address this issue, alkali-activated materials (AAMs) are thereby introduced as an alternative binder to save CO_2 during concrete production [25]. A notable example is ultra-high-performance alkali-activated concrete (UHPAAC) [26], which might effectively mitigate the CO_2 emissions from PC binders while preserving equivalent performances [27–29]. While a few studies have highlighted the positive impact of DS on the mechanical properties of AAMs [30,31], the underlying mechanisms are yet to be fully understood. This research gap offers promising opportunities to investigate the interactions between DS and AAMs, opening pathways to develop more sustainable construction materials utilizing both alternative binders and aggregates.

Inspired by the advances illustrated above, this study explores the potential application of DS as a substitute fine aggregate to SS in producing UHPAAC, with a specific focus on the interactions between aggregates and the binding matrix. DS samples (collected from the desert in Kansu, China) were first sieved into in different particle fractions for characterization, and then blended into UHPAAC mixtures to substitute SS in various volume ratios. The early-stage pore solution chemistry, reaction products, as well as mechanical and microstructural properties of hardened mixtures were further investigated to reveal the interactions between DS aggregate and AAM binders, which have seldom been reported in the literature. Eventually, the effects of utilizing DS on the material cost and environmental impact of UHPAACs were quantitatively assessed. The findings could pave the way for utilizing DS as a supplementary construction material, particularly in AAMs, to further enhance sustainability.

2. Experimental method

2.1. Raw materials

AAM binders used in the current work were prepared through the alkali activation of commercial ground granulated blast furnace slag (BFS), coal fly ash (FA), and silica fume (SF) as precursors. The density of BFS, FA, and SF used in this study are 2.8, 2.32, and 2.2 g/cm^3, respectively. Fig. 1 shows the mineralogical composition of solid precursors, determined with X-ray diffraction (XRD). XRD analysis was performed using a Bruker D8 Advance diffractometer, covering a 2θ range from 10° to 70° with a step size of 0.02° 2θ/s. It was found that BFS and SF are mainly amorphous, whereas FA is composed of various crystalline phases including sillimanite, quartz, hematite, and manganite (Table A1). The surface morphology of solid precursors was observed with a scanning electron microscope (SEM, JEOL JSM-IT800), and the SEM images are presented in Fig. 2(a), (b), and (c). For each test, solid grains were evenly adhered to a conductive tape and coated with a thin platinum layer to enhance conductivity prior to visualization. SEM images were captured using the secondary electron (SE) mode at an accelerating voltage of 10 kV. BFS grains exhibited an angular particle morphology, while FA and SF were observed in spherical shapes.

Moreover, silica sand (SS) with a maximum particle size of 2.36 mm was applied as fine aggregates in this work to prepare UHPAAC. Apart from that, desert sand (DS) collected from Kansu, China was adopted to partially replace silica sand in UHPAAC. DS received was first dried in a ventilated oven at 105 ℃ for 24 h before further characterization. After drying, DS was sieved into different particle fractions and weighed to assess the mass distribution. DS in each fraction was then ground to pass a 63 μm sieve for analyses with XRF and XRD. SS samples were analyzed together without sieving, following identical approaches alongside DS in various fractions. The density of SS and DS as fine aggregates are 2.65 and 2.72 g/cm^3, respectively, as determined in accordance with EN 1097–7. The surface morphology of SS and DS aggregates were observed with SEM, as shown in Fig. 2(d) and (e). DS particles were detected with a smoother and flatter surface morphology in contrast to the angular-shaped SS grains, accompanied by fewer convex or concave regions.

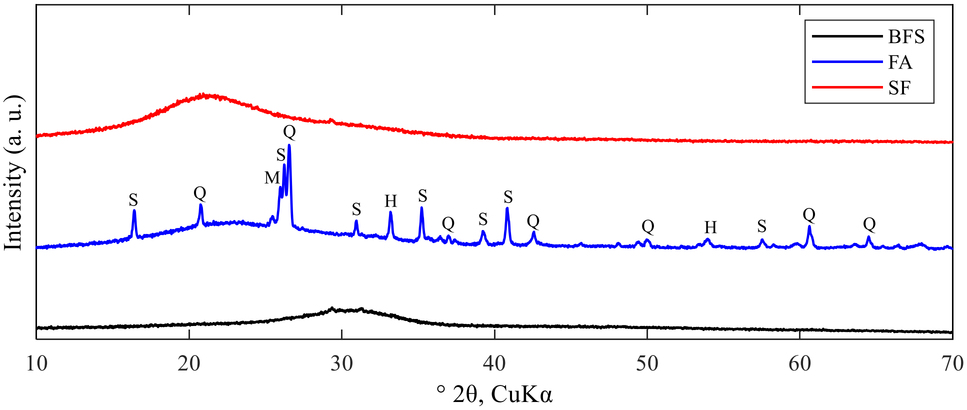

Fig. 1. Mineralogical compositions of solid precursors used in this study by XRD (S-Sillimanite ($Al_2(SiO_4)O$); Q-Quartz (SiO_2); H-Hematite (Fe_2O_3); M-Manganite ($MnO(OH)$)).

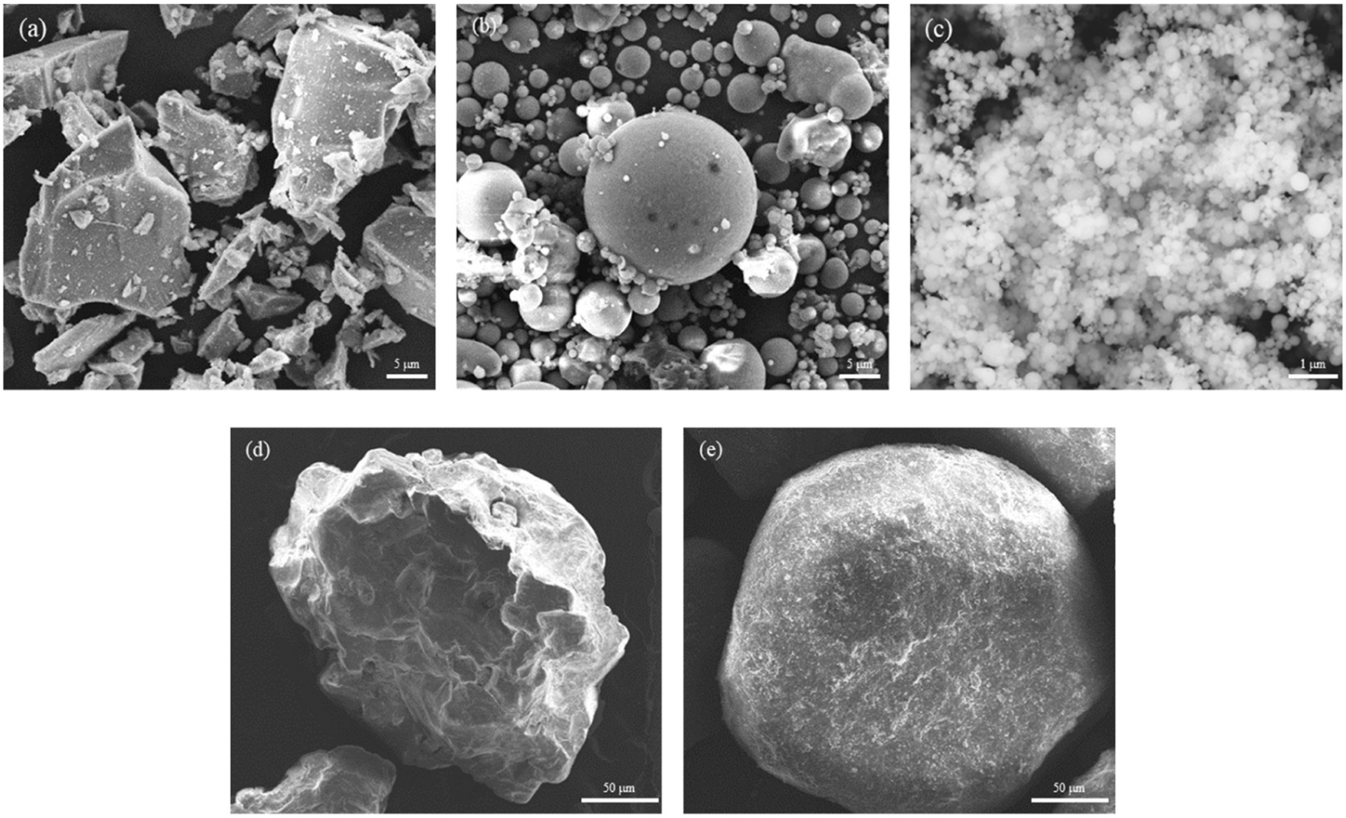

Fig. 2. Surface morphology of solid raw materials (precursors and aggregates) used in this study by SEM (a) BFS; (b) FA; (c) SF; (d) SS;(e) DS.

Table 1
Chemical compositions of raw materials measured by XRF (by wt%).

Precursor	CaO	SiO_2	Al_2O_3	Na_2O	MgO	SO_3	TiO_2	K_2O	Fe_2O_3	MnO	ZnO	Cl	Others
BFS	45.97	27.62	12.91	0.42	7.92	1.65	1.79	0.44	0.43	0.42	-	0.06	0.76
FA	3.41	56.53	29.18	0.40	0.76	0.63	1.60	2.31	4.39	0.04	0.03	-	0.55
SF	-	99.9	-	0.04	0.02	0.02	-	-	-	-	-	0.01	0.01
SS	0.22	90.58	4.8	0.21	0.12	0.21	0.31	2.91	0.42	-	-	-	0.22
DS	6.33	67.29	11.23	1.65	2.91	0.06	0.71	3.0	6.32	-	0.01	0.02	0.47

Table 1 outlines the chemical composition of raw materials used in this study, determined with X-ray fluorescence (XRF). Solid raw materials were finely ground to pass through a 200-mesh sieve and analyzed via a PANalytical Axios spectrometer for XRF measurements. Oxide compositions were quantified using dedicated analytical software. In addition, the particle size distribution of BFS, FA, and SF measured with laser diffraction, as well as the cumulative percentage passing curves for SS and DS, determined through sieving analysis in accordance with the EN 933–1 method, are shown in Fig. 3.

Further, steel fibers (Fig. 4) with a length of 13 mm and diameter of 0.2 mm were used in this study to produce UHPAAC, and the physical features of steel fibers are summarized in Table 2. Alkaline activators were prepared with reagent-grade sodium hydroxide and sodium silicate. Sodium hydroxide anhydrous pearls (> 99 %) and sodium silicate solution (8 % Na_2O, 27 % SiO_2, and 65 % water) were provided by Aladdin Co., Ltd.

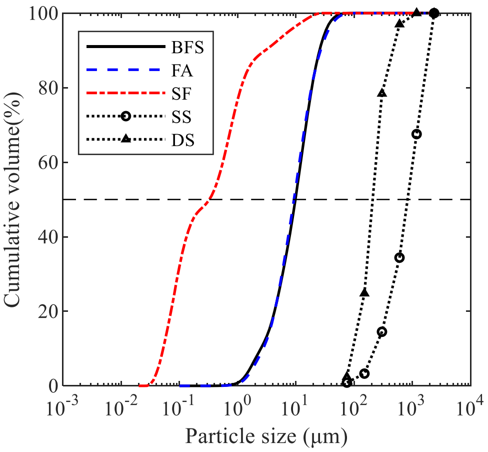

Fig. 3. Particle size distribution of raw materials used in this study.

2.2. Mixture proportions

Details of UHPAAC mixture proportions are presented in Table 3. U1 was designed as the reference mixture prepared with pure silica sand (SS) to achieve the strength demand of UHPAAC as per ASTM C1856 through trial mixes. The binding phases, including solid precursors and alkaline activators were kept consistent among all mixtures in this study. The sodium concentration (Na_2O content by mass of solid precursors) and silicate modulus (Ms, molar ratio between SiO_2 and Na_2O) in activators used in this study were set as 7 % and 0.75, respectively.

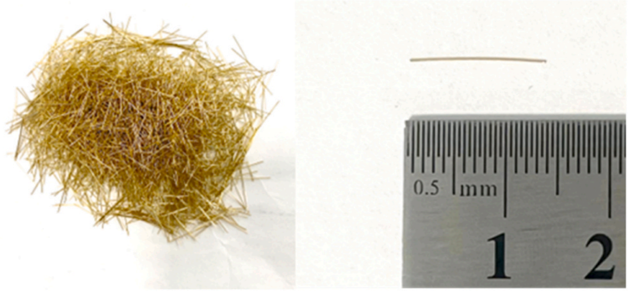

Fig. 4. Steel fibers used in this study.

Table 2
Physical properties of steel fibers used in this study.

Diameter (*d* in mm)	Length (*l* in mm)	Aspect ratio (*l*/*d*)	Density (kg/m^3)	Tensile strength (MPa)	Elastic modulus (GPa)
0.2	13	65	7800	2850	200

Meanwhile, the water to binder (w/b) ratio was fixed at 0.3, and the steel fiber content kept constant at 2 vol% per unit cubic meter of UHPAAC. Further, U2, U3, U4, and U5 were prepared with an increased content of DS (10 %, 30 %, 50 %, and 100 % by volume fractions) to partially replace SS and assess the interaction between AAM binders with different types of aggregates.

Alkaline activators were prepared by dissolving sodium hydroxide pearls and sodium silicate solution into tap water to reach the composition indicated in Table 3. Activator solutions obtained were cooled down to room temperature 24 h before mixing and sealed in plastic bottles to prevent moisture evaporation.

2.3. *Testing program*

2.3.1. *Preparation of UHPAAC*

Fresh UHPAAC mixtures were prepared with a Hobart planetary mixer by following the identical approach outlined below. Solid precursors including BFS, FA, and SF were first dry-blended at low speed (140 ± 5 rpm) for 2 min, followed by the addition of aggregates and intermixed at low speed for another 1 min to reach a homogeneous state. Subsequently, activator solutions were gradually added in 30 s and the mixture was blended at low speed for 3 min. To avoid the agglomeration, steel fibers were slowly introduced by passing through a 6 mm steel sieve in 5 min [32]. Eventually, the mixture was further mixed at high speed (285 ± 5 rpm) for 2 min to better disperse the steel fibers. The sequence of intermixing raw materials took 10 min in total, starting from the wetting of precursors.

Fresh UHPAAC mixtures were then cast into $40 \times 40 \times 160$ mm^3 prisms in two layers, and each layer was compacted on a vibrating table for 15 s to remove the air bubbles. The samples were covered with plastic sheets to prevent the moisture evaporation and placed in a standard curing chamber (20 ± 2 ℃, 95 % relative humidity). Hardened prisms of UHPAAC were demolded after 24 h and transferred into a steam curing device and cured at 90 ℃ for another 24 h.

2.3.2. *Workability*

The workability of UHPAAC mixtures was assessed using the flow table test in accordance with ASTM C1437. Freshly prepared mixtures were immediately placed into a truncated cone mold (top inner diameter 70 mm, bottom inner diameter 100 mm, height 60 mm) and compacted with a steel rod. Once compacted, the cone was removed, allowing the mixture to spread across a flat plate, which was then dropped continuously 25 times. The spread diameter was measured along two perpendicular directions. Notably, all workability tests were performed 12 minutes after wetting the precursors, with the results representing the average of two measurements.

2.3.3. *Pore solution chemistry*

Investigations on the pore solution chemistry were carried out to illuminate the effect of DS inclusions on early-stage activation reactions. After mixing, fresh UHPAAC mixtures were loaded into plastic tubes and centrifugated at 10000 rpm for 5 min to separate the liquid and solid phases while extracting the pore solution. The start of centrifugation was kept constant 12 min after the wetting of precursors among all mixtures. Pore solutions (supernates) obtained were collected with a syringe to pass through a 0.45 μm polyethersulfone membrane filter, and diluted using nitric acid (0.2 vol%) following the method described in [33]. The concentrations of Ca, Al, Si, Na, Mg, and K elements in the pore solution were then immediately analyzed using an inductively coupled plasma - optical emission spectrometry (ICP-OES, Thermo Scientific iCAP 7400).

2.3.4. *Compressive and flexural strength*

The compressive and flexural strength of hardened UHPAAC specimens with different dosages of DS were checked after demolding and steam curing. Tests were conducted in accordance with EN 196–1 using a universal testing machine (Instron 5969) fitted with a 50 kN capacity load cell. The compressive and flexural strength presented are expressed as the average results on three replicate specimens.

2.3.5. *Reaction products*

Fourier transform infrared (FTIR) spectroscopy and XRD analyses were performed on UHPAAC samples after steam curing to evaluate the impact of DS on the reaction products. The hardened specimens were fragmented and immersed in isopropanol for three days to stop the activation reaction [34]. The solid particles were vacuum-dried, then ground with an agate mortar to pass through a series of sieves, during which the relatively coarser grains of aggregate and steel fibers were gently removed [17]. Subsequently, fine powders below 63 μm were used for FTIR and XRD analyses. FTIR spectroscopy was carried out using a Shimadzu IRAffinity-1 spectrometer, scanning from 400 to 4000 cm^{-1} with a resolution of 1 cm^{-1}. XRD tests were conducted using a Bruker D8 Advance diffractometer with Cu-Kα radiation (λ = 1.54 Å), over a range of 2θ between 10° and 70°, with a resolution of 0.02° 2θ/s.

Table 3
Mixture proportions of UHPAACs used in this study.

	Precursors (kg/m^3)			Activators (kg/m^3)			w/b[a]	Aggregates (kg/m^3)		Steel fiber[b] (kg/m^3)
Mix	BFS	FA	SF	Sodium hydroxide	Sodium silicate	Water		SS	DS	
U1	720	160	40	67.44	186.67	189.95	0.3	800	0	156
U2	720	160	40	67.44	186.67	189.95	0.3	720	82	156
U3	720	160	40	67.44	186.67	189.95	0.3	560	246	156
U4	720	160	40	67.44	186.67	189.95	0.3	400	411	156
U5	720	160	40	67.44	186.67	189.95	0.3	0	822	156

[a] Water to binder ratio by mass, and binder is defined as the sum of precursors and solid activators.

[b] Steel fiber content is fixed at 2 vol% of UHPAAC.

2.3.6. Microstructural properties

Hardened UHPAAC specimens after steam curing were split into small pieces for the investigation on microstructural properties. Samples in fragments were then soaked in isopropanol for three days to stop the activation reaction [35], and then subjected to vacuum filtration. Solid residue was dried in a ventilated oven at 40 ℃ for 24 h to eliminate the remaining isopropanol [36].

The microstructures of UHPAAC were visualized using SEM under the backscattered electron (BSE) mode associated with the energy dispersive X-ray spectroscopy (EDS, Oxford Ultim Max 65) analyses. Samples of UHPAAC fragments were epoxy impregnated and subjected to surface smoothing (grinding and polishing) to achieve a surface fineness of 0.25 μm [36]. A thin layer of platinum was coated on the sample surface to improve the conductivity before SEM analyses. BSE images were taken with an acceleration voltage of 10 kV at a working distance of 10 mm.

In addition, the pore structures developed in UHPAAC samples were detected using an AutoPore IV 9510 mercury intrusion porosimetry (MIP). The surface tension of mercury is 0.48 N/m at 20 ℃, whereas the contact angle between the sample surface and mercury was set as 140° [37]. MIP analyses were performed twice to check the repeatability.

2.3.7. Micromechanical properties

To further investigate the interfacial properties, U1 (100 % SS) and U5 (100 % DS) after being exposed to steam curing were selected to assess the bonding between different types of aggregates and the AAM binding matrix. Nanoindentation was conducted to assess the local micromechanical properties along the interfacial transition zone (ITZ) using a Bruker Hysitron TI 950 TriboIndenter, which was fitted with a Berkovich indenter tip (elastic modulus of 1140 GPa and Poisson's ratio of 0.07). The indentation process was conducted following the protocol recommended in previous studies on AAMs [38,39], consisting of three loading steps including (1) loading with a constant rate of 400 μN/s to reach the maximum load of 2 mN, (2) retaining the maximum load for 5 s, and (3) unloading at 400 μN/s. Thereafter, the indentation modulus (M) and hardness (H) can be calculated by following Eqs. (1) and (2) [40], and then the elastic modulus (E) of samples tested can be determined using Eq. (3) [41,42]. For each mix, ten indentations were performed on random ITZ areas with a grid meshing of 8 × 6 points (the spacing was set as 10 μm to prevent interference from adjacent indents [43]) to determine the local indentation modulus and hardness [44].

$$M = \frac{\sqrt{\pi}S}{2\beta\sqrt{A_c}} \tag{1}$$

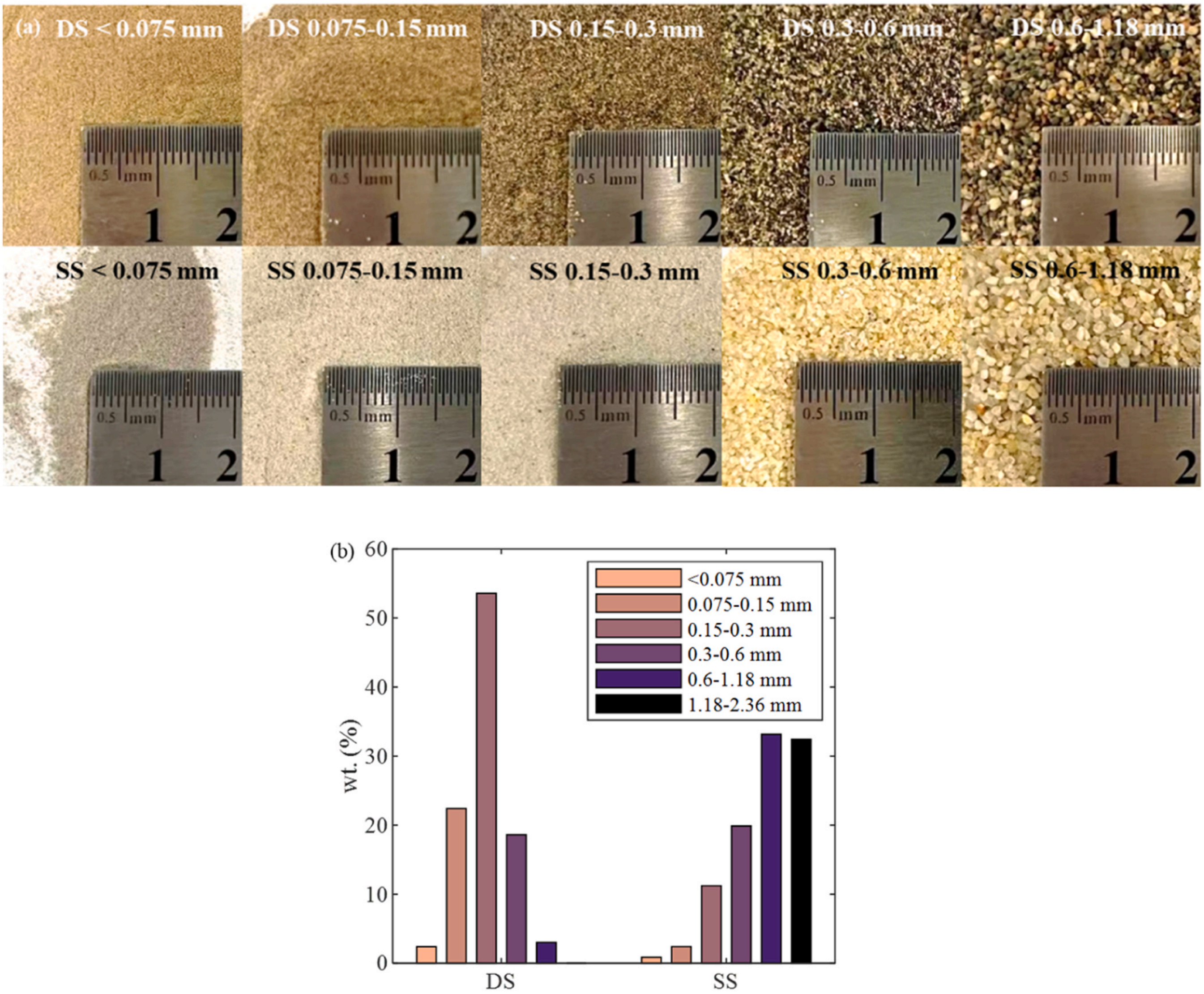

Fig. 5. Sieving analysis on DS and SS (a) Appearance of fine aggregates used in different particle fractions; (b) Mass distribution of DS and SS in different particle fractions.

$$H = \frac{P_{\max}}{A_c} \tag{2}$$

$$\frac{1}{M} = \frac{1-\nu^2}{E} + \frac{1-\nu_{tip}^2}{E_{tip}} \tag{3}$$

where S is the contact stiffness; $\beta = 1.03$ is the shape factor of the Berkovich indenter used in this study; A_c is the contact area; P_{max} is the maximum load occurred during the indentation process; E is the elastic modulus of the sample tested; ν is the Poisson's ratio of the sample tested; $E_{tip} = 1140\text{GPa}$ and $\nu_{tip} = 0.07$ represent the elastic modulus and Poisson's ratio of the indenter, respectively.

3. Results and discussion

3.1. Characterization of desert sand

A sieving analysis was performed on the received DS and SS. The mass percentage in each fraction relative to that of SS is shown in Fig. 5. The results indicate that the overall grain size of DS is much smaller than that of SS, with a significant portion falling into particle fractions between 0.075 and 0.6 mm, revealing a relatively concentrated gradation [8]. Moreover, DS was rarely detected in fractions above 1.18 mm. Table 4 presents the chemical compositions of DS in different fractions. Results have illustrated that the content of the primary compound SiO_2 gradually decreases with the reduction in DS grain size. This is accompanied by slight increases in other elemental content in finer DS particles. In particular, the DS in various fractions were found to contain higher levels of aluminum content (Al_2O_3), along with a few alkali and alkali-earth metal oxides (e.g., Na_2O, CaO, and MgO), indicating potential suitability for synthesizing AAM binders [45].

The mineralogical compositions of DS and SS were analyzed using XRD, as shown in Fig. 6. SS is mainly composed of quartz, with minor albite, muscovite, and orthoclase phases present as well. Extensive distributions of quartz phases were also found in DS samples. In addition to the phases detected in SS, kaolinite, calcite, portlandite, and tremolite were also identified in DS, revealing a more complex composition. Furthermore, minor humps between 20° and 30° were detected in DS samples, in contrast to the relatively flat profile observed in this region in SS. These humps suggested the presence of amorphous aluminosilicate phases in DS [46], which might potentially contribute to the subsequent alkali activation reactions.

3.2. Workability

The workability of fresh UHPAAC mixtures was evaluated using flow table tests. Results of the flow diameters are depicted in Fig. 7. When 10 % of DS was incorporated to replace SS, it was observed that the flow diameter of U2 increased by 4.9 % compared to that of U1. As shown in Fig. 2(d) and (e), the smoother surface of DS, in contrast to the angular-shaped SS particles, contributed to a fluidizing effect by reducing the interparticle friction [47,35]. In addition, DS with finer particles may fill in the interparticle voids and improve the packing in fresh mixtures [12]. Thereby, U2 demonstrated superior workability compared to the reference mixture U1. However, an increased content of DS adversely affected the workability of fresh UHPAAC mixtures. The flow diameter progressively decreased in U3, U4, and U5, as illustrated in Fig. 7. This can be attributed to the higher water absorption rate of DS compared to SS aggregates [47,48]. As a result, the further increase of DS content reduced the free water content in the fresh mixtures, which is essential for lubrication [34], thereby leading to a reduction in the flow diameter.

3.3. Pore solution chemistry in fresh mixtures

The chemical compositions of pore solutions extracted from U1, U2, and U4 were analyzed using ICP-OES to investigate the impact of DS on early reaction mechanisms. As shown in Table 5, the calcium content in U2 increased by 15.9 % compared to U1 when 10 vol% of SS was replaced with DS. Moreover, the calcium ion concentration in the pore solution of U4 further improved with a higher DS content. A similar trend was observed for the Al element, indicating the beneficial role of DS during alkali activation to promote the formation of C(N)-A-S-H reaction products [30,31]. By contrast, the ionic strength of Na and Si, which were abundant in the activator solutions, generally decreased with the incorporation of DS, indicating their consumption and the formation of early reaction products. In essence, the dissolution of various elemental species from DS grains effectively enhanced the ionic concentration in the pore solution, thereby promoting early reaction kinetics from a chemical perspective [49,35].

3.4. Compressive and flexural strength

After 1-day standard curing and an additional 1-day of steam curing, the mechanical properties of hardened specimens were tested on hardened prisms. The results of compressive and flexural strength are displayed in Fig. 8. It was observed that mixtures U1, U2, U3, and U4 met the minimum compressive strength of UHPC as specified in ASTM C1856, while the strength of U5 was slightly below the threshold. Among all mixtures, U2 exhibited the highest compressive and flexural strength. By replacing 10 vol% SS with DS, the ultimate compressive strength developed in U2 was enhanced by about 20 % compared to that of U1. Similar results have been reported in previous literature, attributed to the partial dissolution of DS, which facilitates the formation of C-(A-)S-H reaction products [30,31]. However, the boosting effect became less pronounced as the ultimate strength of U3, U4, and U5 progressively declined with further increases in the DS replacement ratio. Similar trends were observed in the flexural strength of hardened specimens. Subsequent microstructural investigations will provide additional insights into the variations in mechanical properties, by exploring the interactions between different types of aggregates and AAM binders.

3.5. Microstructural properties

Fig. 9 illustrates representative BSE images of hardened UHPAAC samples, where various phases can be distinguished. Coarser, dark grey grains correspond to aggregates such as SS and DS, while finer, angular-shaped grains with lighter grey tones indicate undissolved BFS particles. Spherical grains with internal pores embedded within the binding matrix are associated with FA, whereas microspheres with significantly finer grain sizes represent SF as precursors. In addition, the black areas

Table 4
Chemical compositions of DS in different particle fractions and SS measured by XRF (by wt%).

Particle size (mm)	CaO	SiO_2	Al_2O_3	Na_2O	MgO	SO_3	TiO_2	K_2O	Fe_2O_3	MnO	ZnO	Others
< 0.075	9.04	59.88	14.08	1.38	3.66	0.26	1.07	2.90	6.89	0.12	0.02	0.70
0.075–0.15	7.75	61.08	14.45	1.50	3.56	0.13	0.84	3.14	6.92	0.12	0.02	0.49
0.15–0.3	6.67	60.86	15.40	1.42	3.68	0.11	0.75	3.45	7.19	0.14	0.01	0.32
0.3–0.6	5.20	70.16	11.72	1.78	2.49	0.09	0.52	2.69	4.87	0.12	0.01	0.35
0.6–1.18	4.19	73.26	10.97	2.01	2.11	0.10	0.40	2.55	3.91	0.08	0.01	0.41
SS	0.22	90.58	4.8	0.21	0.12	0.21	0.31	2.91	0.42	-	-	0.22

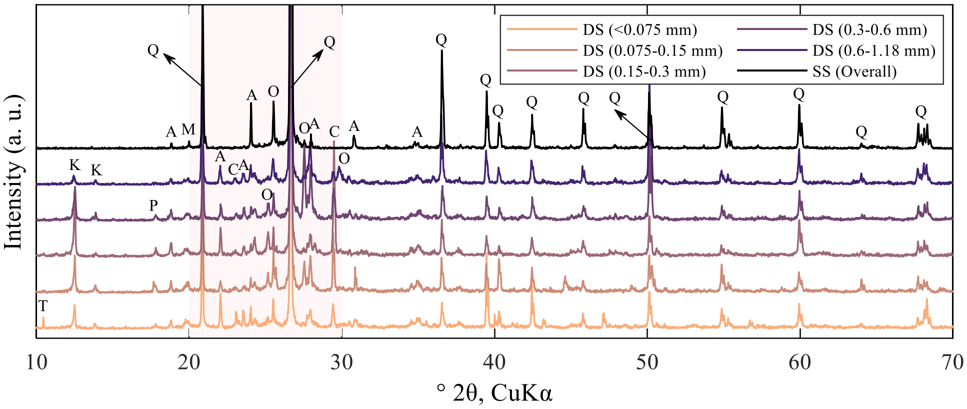

Fig. 6. Mineralogical compositions of DS in different particle fractions and SS used in this study by XRD (Q-Quartz (SiO_2); A-Albite ($NaAlSi_3O_8$); K-Kaolinite ($Al_4(Si_4O_{10})(OH)_8$); T-Tremolite ($Ca_2Mg_5(Si_8O_{22})(OH)_2$); M-Muscovite ($KAl_2(AlSi_3O_{10})(OH)_2$); P-Portlandite ($Ca(OH)_2$); O-Orthoclase ($KAlSi_3O_8$); C-Calcite ($CaCO_3$).

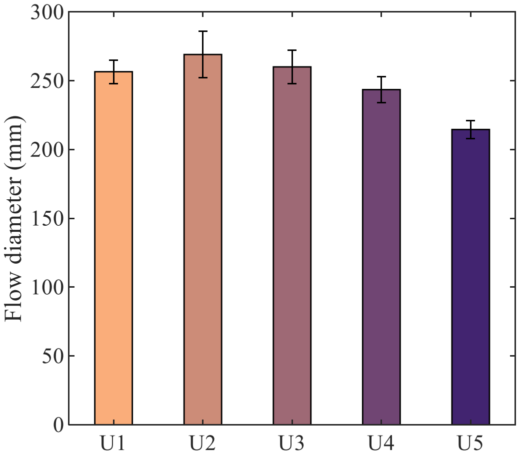

Fig. 7. Flow diameters of fresh UHPAAC mixtures.

Table 5
Element concentration in the pore solutions extracted in fresh UHPAAC (mol/L).

(mol/ L)	Ca	Si	Al	Mg	Na	K
U1	0.574 ± 0.034	9.600 ± 0.340	0.297 ± 0.015	0.144 ± 0.008	8.250 ± 0.106	0.095 ± 0.003
U2	0.600 ± 0.029	7.770 ± 0.120	0.343 ± 0.010	0.171 ± 0.020	6.871 ± 0.320	0.099 ± 0.001
U4	0.649 ± 0.039	7.900 ± 0.100	0.448 ± 0.011	0.209 ± 0.010	7.290 ± 0.138	0.099 ± 0.002

indicate the presence of local microcracks and pores, which were more frequently detected in mixtures with a higher content of DS, leading to declined mechanical properties compared to other mixtures (Fig. 8). Furthermore, aggregates in U5 (100 % DS) displayed a distinct morphology compared to those in U1 (100 % SS). In contrast to the smooth boundary between the binding matrix and SS aggregates observed in U1 (Fig. 9(a)), the aggregates in U5 were characterized by an etching front located at the interfacial areas and extending towards the inner core of the aggregate (indicated with the dashed rectangular in Fig. 9(d) and (e)). The etching front featured a porous and rough texture along the edges of DS grains, in contrast to the dense and smooth matrix observed on SS particles. Moreover, the porous morphology implies the local dissolution of DS upon contact with AAM binders, which is supported by the ICP results (Table 5). However, SS and DS are difficult to distinguish in BSE images (Fig. 9) due to similarity in compositions and geometric conditions for imaging. Further studies on U1 (100 % SS) and U5 (100 % DS) were conducted to reveal the interfacial transition zone (ITZ) properties using different types of aggregates, which will be addressed in Section 3.7.

In addition, MIP tests were conducted to analyze the pore structures in hardened samples with different DS contents [50], as shown in Fig. 10. According to literature, pore structures in hardened cementitious composites can be categorized based on pore size into (1) gel pores (<10 nm), (2) transition pores (10–100 nm), (3) capillary pores (100–1000 nm), and (4) macro-pores (>1000 nm) [51]. The majority of pores, as depicted in Fig. 10, were found to have a diameter below 10 nm. Fig. 10 (b) illustrates the cumulative porosity of hardened samples in different pore size fractions, revealing a progressive increase in overall porosity with higher DS content. This increase is linked to a significant rise in gel pores and a slight reduction in macro-pores. U5 was detected with the highest porosity of 8.5 %, while all UHPAAC mixtures exhibited a relatively dense microstructures as revealed by the cumulative porosity. Complete substitution of SS with DS led to a 109.64 % increase in gel pores in U5 compared to U1, possibly ascribed to the etched areas observed on the DS outer surfaces (Fig. 9). On top of that, DS with smaller grains compared to SS may result in the formation of numerous interfaces between aggregate grains and the binding matrix from a microstructural perspective. This could lead to higher local porosity due to the 'wall effect' of packing solid binder grains against the relatively flat aggregate surface [52,53], resulting in a decline in mechanical properties in hardened mixtures with higher DS substitution levels (Fig. 8).

3.6. Reaction products

After steam curing, reaction products in UHPAAC samples were analyzed using FTIR and XRD techniques. In Fig. 11 (a), the FTIR spectra displayed several characteristic absorption bands. Peaks at around 970 and 475 cm^{-1} correspond to the asymmetric stretching and bending vibrations of Si-O bonds [54], respectively, which are indicative of alkali activation reactions [55]. In addition, peaks at 3450 and 1640 cm^{-1} represent the bending vibration of O-H bonds, suggesting the presence of chemically bound water along with the activation reaction [56]. Furthermore, a minor peak at about 1425 cm^{-1} is attributed to the vibration of O-C-O bonds, implying the formation of carbonated phases in reaction products. It was observed that the absorption band at 475 cm^{-1} gradually shifted towards lower wave numbers with a higher substitution level of DS. Meanwhile, the band at 970 cm^{-1} shifted to higher wavenumber regions (leftwards, as shown in Fig. 11 (a)), indicating a reduced incorporation of Al species into the aluminosilicate tetrahedra within the reaction products, as reported by Zhang et al. [57]. Aside, XRD patterns of hardened mixtures are shown in Fig. 11 (b), with quartz phases being predominant among all mixtures. A significant diffuse

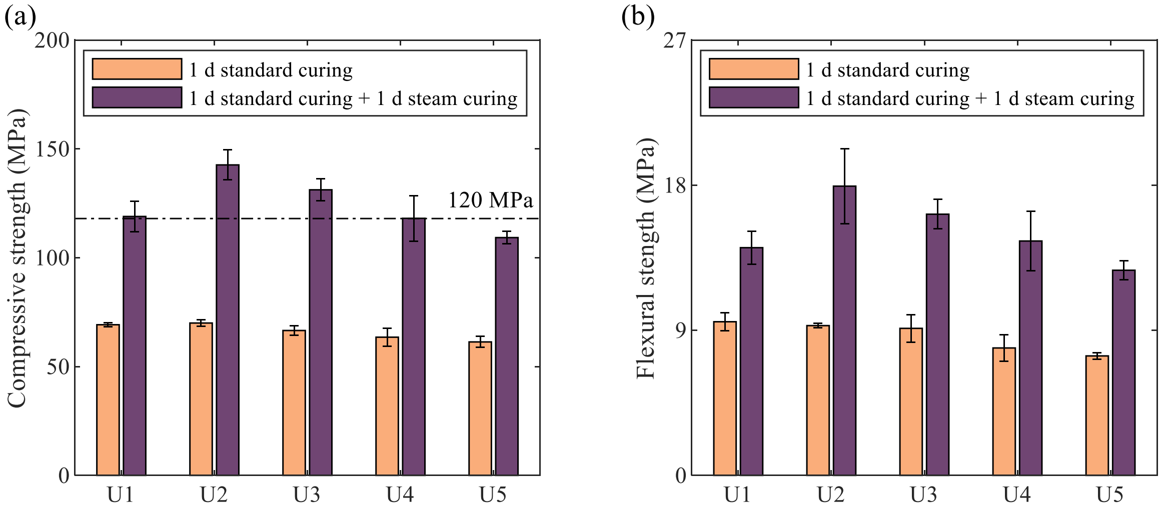

Fig. 8. Mechanical properties of UHPAAC specimens (a) Compressive strength; (b) Flexural strength.

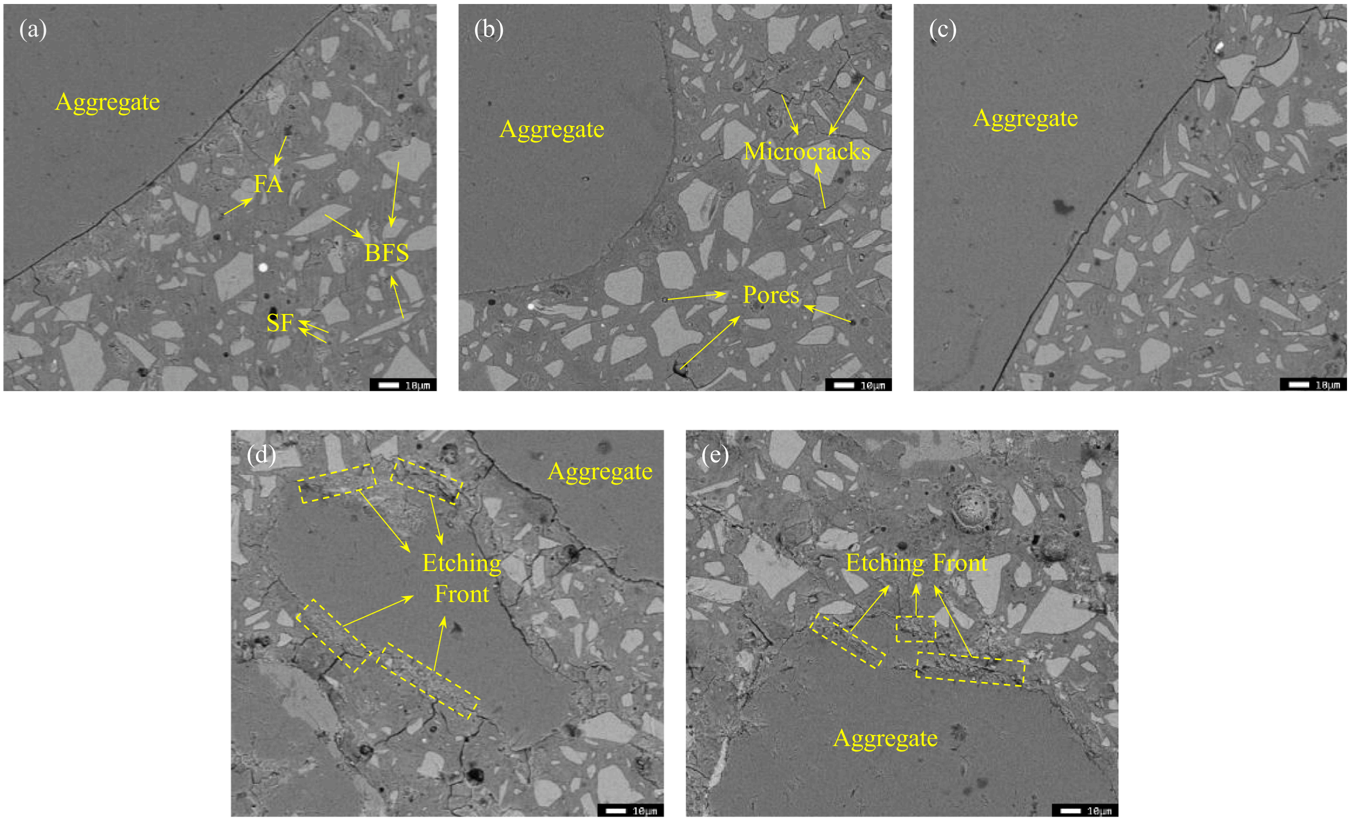

Fig. 9. Characteristic BSE images of microstructures in hardened UHPAAC mixtures (500 × magnification) (a) U1; (b) U2; (c) U3; (d) U4; (e) U5.

hump between 29° and 33° indicates the formation of C-(A-)S-H phases as the primary reaction products in high-calcium AAMs [58]. XRD analyses only provided limited information on the reaction products due to the presence of aggregate fractions (i.e., the predominance of quartz phases), which can hardly be completely removed during the sample preparation. Further investigations were conducted to understand the effect of DS on the alkali activation reaction.

EDS analyses were conducted on the interparticle reaction products to evaluate the impact of DS on the alkali activation reaction, as shown in Fig. 12. The results of atomic ratios presented in Table 6 were calculated as the average of 20 random spots on BSE images (Fig. 9). It's important to note that the spots for EDS analyses were chosen at least 5 μm away from the aggregates and undissolved precursor grains to eliminate their effects on the reaction products [52,59]. It was found that the reaction products in U1 exhibited the highest Ca/Si ratio of 0.629 among all mixes, which progressively declined with more DS incorporated. By replacing 10 vol% SS with DS, the Ca/Si ratio of U2 decreased by 6.3 % compared to U1, indicating an enhanced binding capacity of C-(A-)S-H reaction products due to the decreased mean silicate chain length of aluminosilicate tetrahedrons [60,61]. As a result, the strength of U2 was significantly improved compared to U1, as illustrated in Fig. 8. However, further increases in the DS substitution ratio inversely led to a reduction in mechanical properties in hardened specimens, contrary to the observed trend. Similar results have been

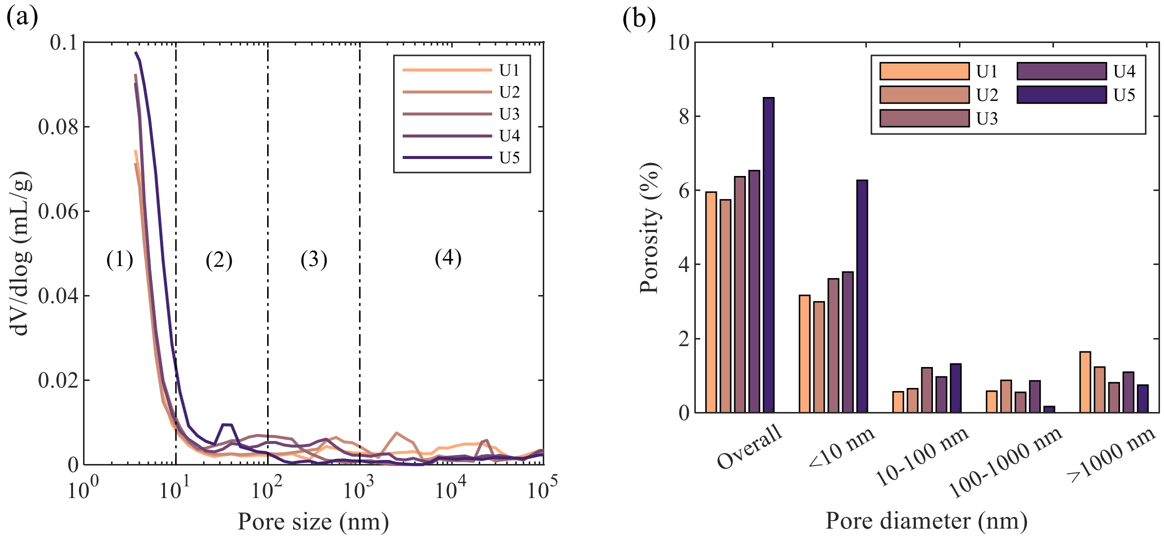

Fig. 10. Pore structures in hardened samples detected by MIP (a) Pore size distribution curves; (b) Cumulative porosity.

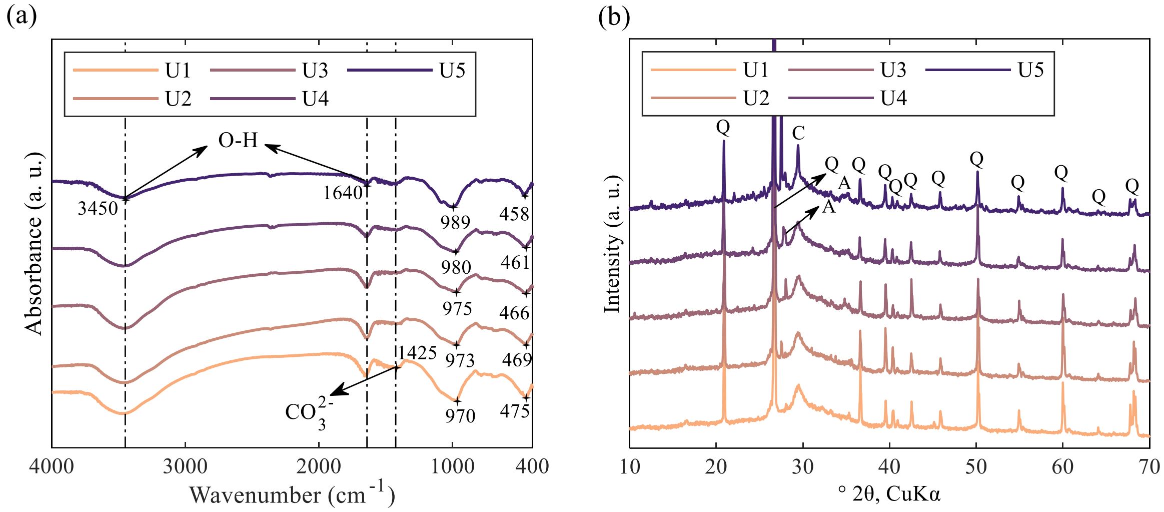

Fig. 11. Characterization of reaction products in UHPAAC samples after steam curing (a) Results of FTIR analyses; (b) Results of XRD analyses (Q-Quartz (SiO_2); A-Albite ($NaAlSi_3O_8$); C-Calcite ($CaCO_3$).

reported in previous works using DS as an substitute material to produce cementitious composites [18,62,48], which will be further discussed by subsequent investigations on the micromechanical properties. Meanwhile, the Al/Si ratio in the reaction products also reduced with a higher DS content, consistent with the modifications in aluminosilicate tetrahedron structures as confirmed by the FTIR results (Fig. 11 (a)). Eventually, no apparent variations were observed in the Na/Si and Mg/Al ratios in reaction products.

3.7. ITZ properties

Investigations were conducted on U1 and U5 (with 100 % SS and DS, respectively) to understand the interactions between different types of aggregates and AAM binders, with a specific focus on the interfacial transition zone (ITZ). EDS mapping and line scanning were performed on U1 and U5 to explore the elemental distribution around the ITZ areas, as depicted in Fig. 13. The analysis revealed that Si was the predominant element in both SS and DS aggregates, consistent with the high quartz content indicated in Fig. 6. Apart from that, DS aggregates showed a higher distribution of Ca, Al, Mg, and Na elements compared to SS, aligning with the results of XRF analyses (Table 4). By using either SS or DS, as explored by the line scanning results (Fig. 13), the concentration of Si element maintained stable at a relative high level in aggregate regions, attributed to the abundant quartz content in both types of aggregates. In contrast, the elements Ca, Al, Mg, and Na were detected at low levels within the aggregate regions but showed a sharp increase at the aggregate-binder interfaces, indicating the formation of reaction products (C-A-S-H and N-A-S-H gels) [63]. Further, the matrix of SS demonstrated a higher Si content compared to DS. In the meantime, Ca, Al, and Si elements were observed to dissolve more significantly from DS particles into the ITZ areas than those from SS, aligning with the ICP results presented in Table 5. These observations further highlight the beneficial role of DS in the alkali activation reaction by supplying calcium and aluminosilicate species as a secondary source in addition to precursors.

The nanoindentation test results are depicted in Fig. 14, displaying contour maps that offer insights into the local micromechanical properties of U1 and U5 samples. On top of that, Fig. 15 illustrates the box plot of micromechanical properties derived from the nanoindentation tests, categorizing aggregate, ITZ, and binder areas based on elastic modulus and hardness. Specifically, aggregates with a notably higher elastic modulus are clearly discernible from the warm colors in Fig. 14.

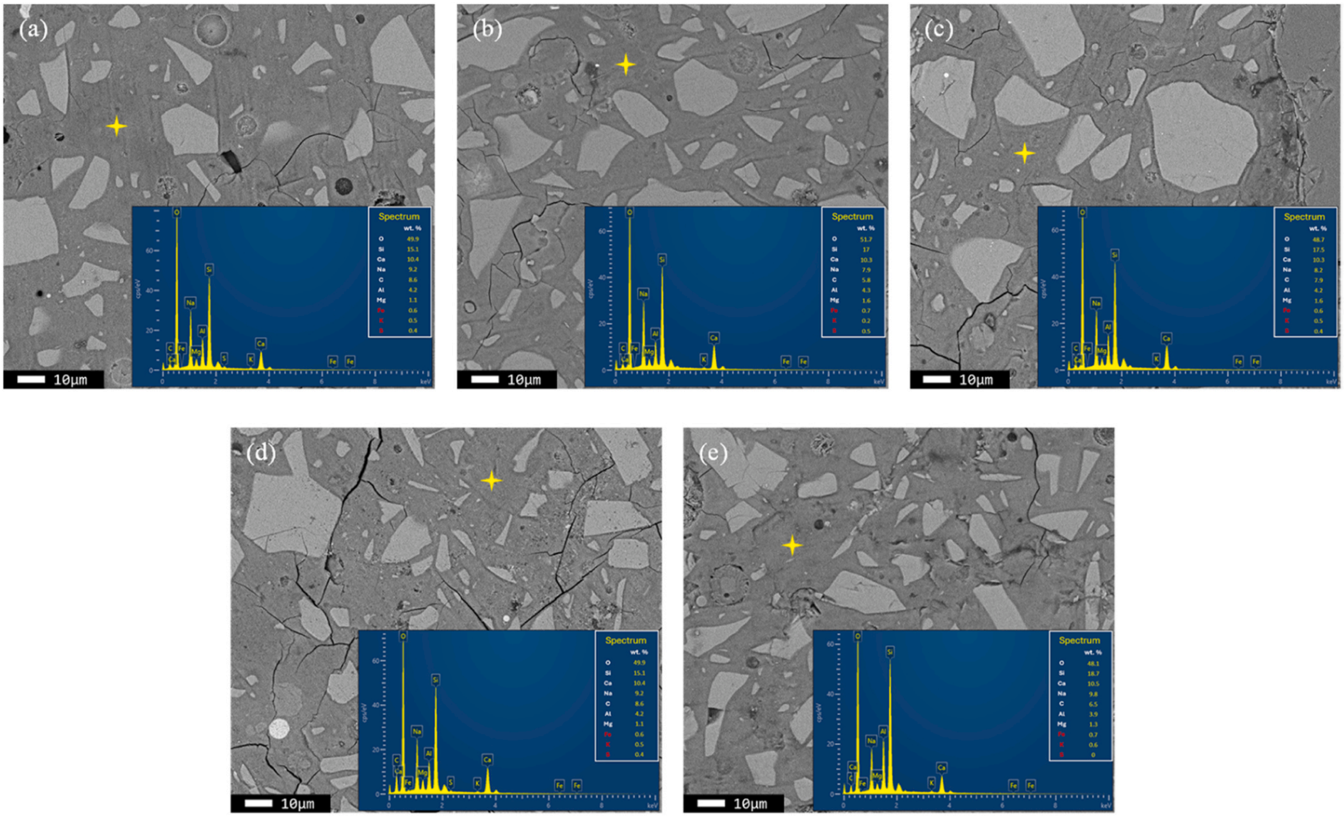

Fig. 12. Characteristic EDS spectra of hardened UHPAAC mixtures (1000 × magnification) (a) U1; (b) U2; (c) U3; (d) U4; (e) U5.

Table 6
Average atomic ratios obtained by EDS analyses.

	Ca/Si	Al/Si	Na/Si	Mg/Al
U1	0.629 ± 0.061	0.261 ± 0.032	0.339 ± 0.046	0.442 ± 0.178
U2	0.596 ± 0.026	0.256 ± 0.026	0.545 ± 0.143	0.371 ± 0.120
U3	0.582 ± 0.022	0.236 ± 0.022	0.437 ± 0.078	0.383 ± 0.098
U4	0.560 ± 0.082	0.217 ± 0.057	0.397 ± 0.119	0.437 ± 0.194
U5	0.555 ± 0.022	0.191 ± 0.070	0.577 ± 0.033	0.468 ± 0.211

Moreover, data for ITZ areas was collected within the distance of 20 μm to the edge of aggregate particles as recommended in [44], while the remaining areas were classified as AAM binders.

SS grains exhibited superior micromechanical features compared to DS grains, which can be attributed to the inherent material properties of both aggregates. The presence of local defects on the surface of DS grains (i.e., the etching front et observed in Fig. 9), due to the dissolution of multiple ionic species (Table 5) may have contributed to the decrease in mechanical properties. Thereby, the elastic modulus and hardness of aggregate phases in U1 were detected approximately 9 % and 19 % higher than those of U5, respectively. Similar trends were observed in ITZ areas, indicating stronger bonding between AAMs and SS compared to DS. This could be ascribed to the smoother surface of DS, as presented in Fig. 2, attenuating the adhesion between aggregates and binder. Further, the results of elastic modulus and hardness in AAM binders were more scattered due to the complex phase assemblage (including reaction products, undissolved precursors, pores, and voids). It was found that U5 exhibited higher elastic modulus and hardness in areas representing binder phases than U1, suggesting the positive contribution of DS, as shown in Table 6. Results are in parallel with the lower Ca/Si ratio detected in the reaction product of U5 compared to U1 (Table 6), leading to the modification of reaction products with better micromechanical properties [61].

Overall, the effect of DS on the mechanical properties of AAMs can be explained through several aspects related to the modification of interactions between aggregate and binder phases. On one hand, the reactive alkali and alkali-earth metals, as well as aluminosilicate species embedded in DS grains, could be released through interaction with AAM binders (Table 5), contributing to the alkali activation reaction and modifying the reaction products (Table 6). Nevertheless, the inclusion of DS with a smaller grain size on the other hand created numerous interfaces, serving as the weak link between aggregates and binder [64, 65]. This is associated with an increase in the microstructural porosity as revealed in Fig. 10. Moreover, results of nanoindentation tests have further demonstrated the poorer micromechanical features of ITZ around DS compared to that of SS (Fig. 15), ascribed to the inherent flat surface (Fig. 2) of DS as well as the porous etching front (Fig. 9) formed through alkali activation reactions. Eventually, DS with a relatively concentrated gradation compared to SS also adversely affected the material packing, leading to a decline in the mechanical strength with a higher DS replacement ratio. In summary, there exist competing mechanisms as illuminated above, depending on the substitution level of SS with DS. U2 with 10 % DS exhibited the highest strength among all mixtures due to the positive chemical effects to contribute to the alkali activation reaction. However, higher dosages of DS in turn created more physical defects (etching fronts observed in Fig. 9) in ITZ areas, causing a localized reduction in micromechanical properties and further decreasing the strength in U3, U4, and U5.

3.8. *Environmental impact analysis*

A literature survey was conducted to quantitatively assess the environmental benefits of incorporating DS into the mix design for producing UHPAACs. Material sustainability indicators (MSIs), specifically embodied energy and CO_2 emissions, were calculated based on the raw materials used in the mixture proportions. The data supporting these

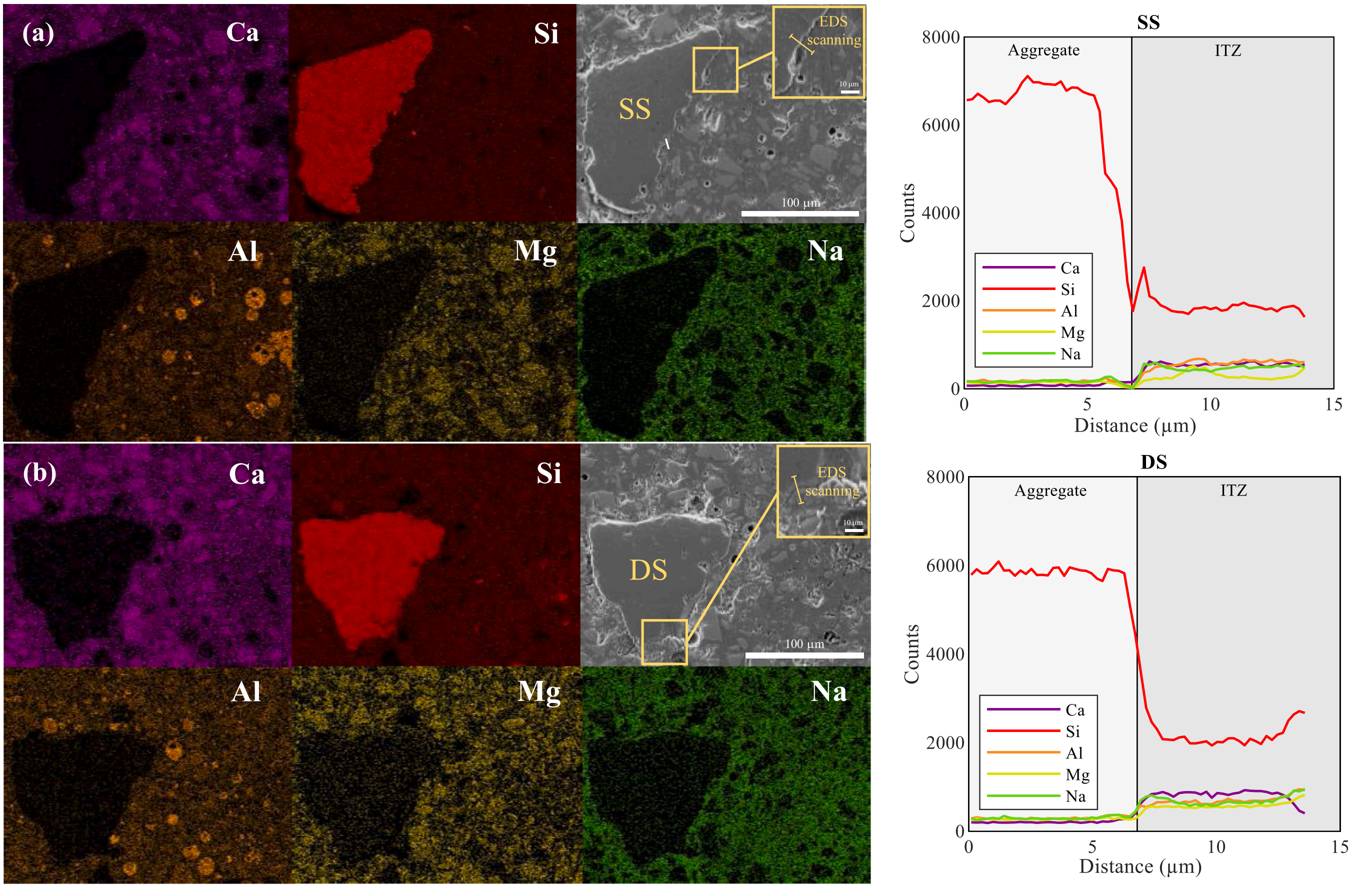

Fig. 13. EDS mapping and line scanning on UHPAAC samples (a) U1 with 100 % SS; (b) U5 with 100 % DS.

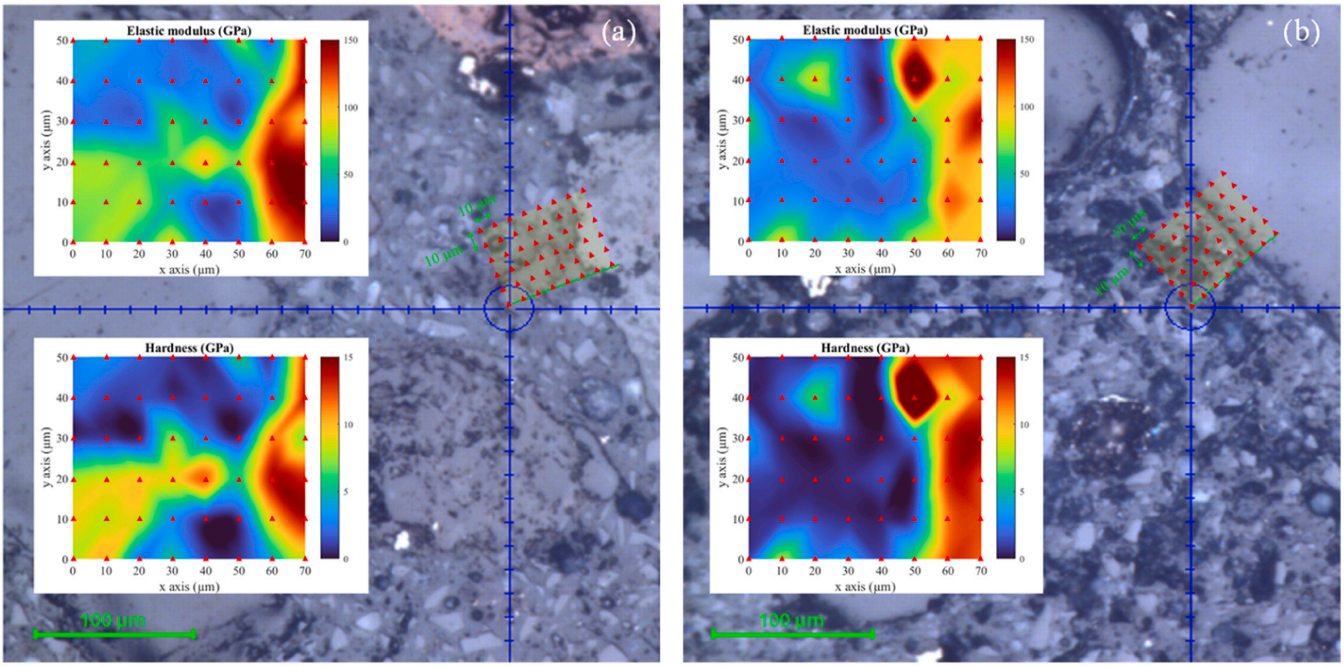

Fig. 14. Results of representative nanoindentation tests (a) U1 with 100 % SS; (b) U5 with 100 % DS.

calculations are detailed in Table 7. It is important to note that the MSIs in this study focus on the specific costs associated with raw material acquisition and the commercial production phase, rather than a full life cycle assessment covering the entire service life [66,67]. Furthermore, in line with Wang et al.'s proposal [68], the CO_2 emissions per kilogram of desert sand were assumed to be zero due to its abundant availability, with only transportation emissions being considered. To enhance clarity and comparability, the results were normalized to the unit compressive

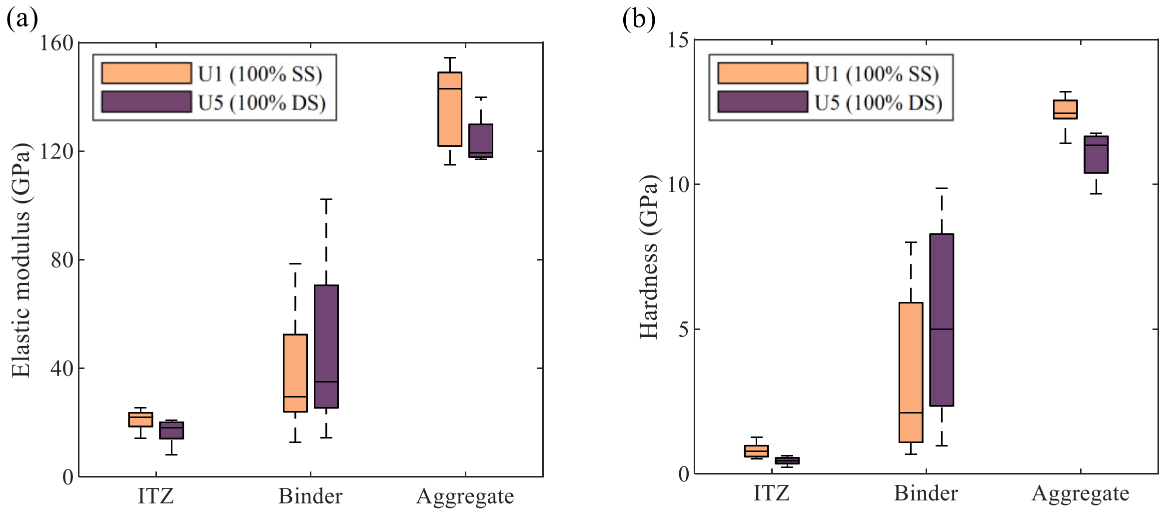

Fig. 15. Box plot of micromechanical properties obtained from the nanoindentation test (a) Elastic modulus; (b) Hardness.

Table 7
Inventory of embodied energy and CO_2 emissions of raw materials to produce UHPAAC from literature.

	Embodied energy (MJ/kg)	CO_2 emission (kg/kg)	Ref.
BFS	1.59	0.02	[69]
FA	3.291	0.362	[70]
Metakaolin	2.5	0.43	[71]
SF	0.1	0.024	[72]
SS	0.15	0.005	[73]
Quartz	0.85	0.023	[74,75]
DS	0.1	0	[68]
Steel fiber	20.56	1.49	[69]
Sodium hydroxide	9.5	0.75	[76]
Sodium silicate	9.4	0.671	[77]
Water	0.01	0	[69]

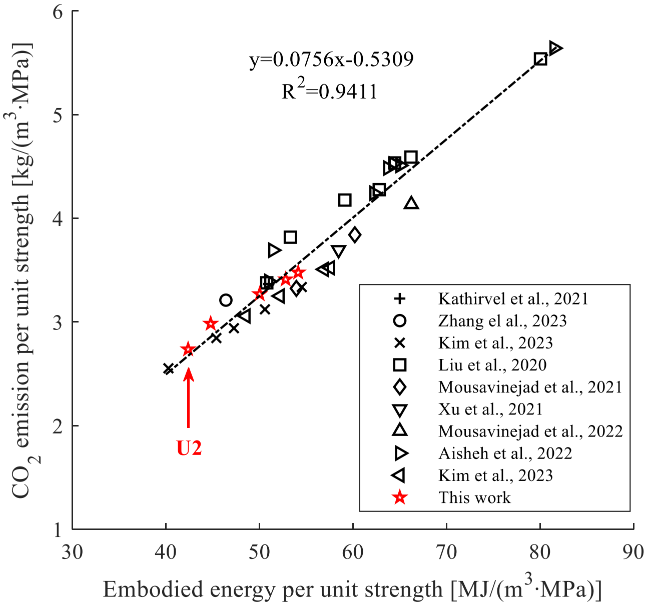

Fig. 16. Material sustainability indicators of raw materials for producing unit cubic meter of UHPAAC, in comparison with mixture proportions reported in the literature [75,78–85] (CO_2 emission vs. embodied energy per unit compressive strength in MPa).

strength of the UHPAAC mixtures. Fig. 16 illustrates a clear linear relationship between embodied energy and CO_2 emissions, emphasizing a significant proportional correlation. Among the mixtures analyzed, U2 with 10 % DS exhibited the lowest CO_2 emissions and embodied energy per unit compressive strength. Furthermore, the mixtures in this study generally showcased competitive MSI levels compared to those reported in previous literature, underscoring the environmental advantages of incorporating DS in UHPAAC mixtures. Notably, the substantial benefits of DS may be more pronounced in regions where natural aggregate resources are scarce and heavily reliant on imports [5,6], despite SS having relatively lower embodied energy compared to other raw materials. In addition, Table 7 underlines that steel fiber accounts for the most significant portion of both embodied energy and CO_2 emission among all raw materials. Future research is encouraged to explore the use of recycled fibers to further mitigate the environmental impact of UHPAAC [67].

4. Conclusions

This study investigates the potential use of desert sand (DS) as a partial replacement for natural silica sand (SS) in ultra-high-performance alkali-activated concrete (UHPAAC). The DS was initially analyzed in different particle size fractions and then incorporated into UHPAACs to substitute SS in varying volume ratios. Detailed characterizations were carried out on the pore solution chemistry, mechanical and microstructural properties, as well as the reaction products of the UHPAAC samples, leading to the following conclusions based on the obtained results:

- DS samples were characterized by a flat and smooth surface morphology, in contrast to the angular-shaped SS grains. Moreover, the DS samples exhibited finer grain sizes, and a more concentrated gradation compared to the SS samples. In addition to the predominant quartz content, minor phases of kaolinite, calcite, and tremolite were detected in the DS samples, accompanied by increases in amorphous calcium and aluminosilicate species in comparison to the SS samples.
- The flow diameter of the mixture containing 10 % DS increased by 4.9 % compared to the reference mix, attributed to its smoother surface morphology compared to SS. However, further increases in DS content reduced workability due to its higher water absorption rate.
- Replacing 10 vol% of SS with DS in the fresh UHPAAC mixture improved the calcium content in the pore solution by 15.9 %, with a

more pronounced effect at higher dosages. The substitution also led to increases in the concentrations of Al, Si, Mg, and K elements. DS has facilitated the early-stage alkali activation reaction, acting as an additional source of various ionic species.

- The highest compressive strength was detected in the mixture with 10 vol% DS, which was improved by about 20 % compared to the reference made of pure SS, reaching 148.13 MPa after steam curing. However, further increases in DS substitution levels have resulted in an adverse effect to reduce the mechanical strength of hardened specimens.
- Characterization of reaction products has confirmed the positive contribution of DS, leading to a lower Ca/Si ratio and less Al-uptake in aluminosilicate tetrahedrons, which aligned with the increase in mechanical strength in mixtures with 10 vol% DS. On the other hand, DS with smaller grain sizes created numerous interfaces with the binding matrix to improve the microstructural porosity in the hardened samples, which is correlated to the reduction in strength with higher DS substitution levels.
- Nanoindentation tests on samples with pure SS and DS have explored the distinctive micromechanical properties by using different types of aggregates. The local elastic modulus of AAM binders around DS was improved by about 25 % compared to that of SS. However, samples with DS were featured with declined elastic modulus and hardness in the aggregate and interfacial transition zone (ITZ) areas due to the presence of more physical defects.
- DS showed notable environmental advantages in UHPAACs. The mixture containing 10 % DS achieved the lowest embodied energy and CO_2 emissions per unit compressive strength among the UHPAACs tested, while the mixtures studied generally exhibited lower environmental impacts compared to those documented in the literature. However, steel fibers emerged as the primary contributor to environmental impacts, highlighting a critical area for future research aimed at minimizing the environmental footprint of UHPAACs.

CRediT authorship contribution statement

Yao Jie: Resources, Investigation. **Sun Yubo:** Writing – review & editing, Methodology, Investigation. **Zhong Jing:** Writing – review & editing, Supervision, Funding acquisition. **Zhang Ming:** Writing – original draft, Methodology, Investigation. **Hu Pengfei:** Writing – original draft, Investigation. **Sun Shangyu:** Writing – original draft.

Declaration of Competing Interest

The authors declare that they have no known competing financial interests or personal relationships that could have appeared to influence the work reported in this paper.

Acknowledgements

This research was funded by the National Natural Science Foundation of China (Grant No. 52073073). Grateful acknowledgment is also extended to China State Construction International Holdings Limited for the financial support (Project No. CSCI-2023-Z-11: Research on Key Technologies of Modular Concrete School Building Products, and CSCI-2023-Z-26: Research and Application of Ultra-Low Energy Building Envelope Systems Based on Vacuum Insulation Panels).

Appendix

Table A1
The prominent peaks of mineral phases presented in this study

Mineral phase	Chemical composition	Prominent peaks 2θ (°)
Albite	$NaAlSi_3O_8$	22.0, 27.8, 30.3, 34.9
Calcite	$CaCO_3$	23.1, 29.4
Hematite	Fe_2O_3	33.2, 54.1
Kaolinite	$Al_4(Si_4O_{10})(OH)_8$	12.4
Manganite	MnO(OH)	25.8
Muscovite	$KAl_2(AlSi_3O_{10})(OH)_2$	19.8
Orthoclase	$KAlSi_3O_8$	25.5
Portlandite	$Ca(OH)_2$	18.1
Quartz	SiO_2	20.8, 26.6, 36.5, 39.4, 42.4, 50.1, 54.8, 60.0, 68.2
Sillimanite	$Al_2(SiO_4)O$	16.4, 26.5, 31.3, 35.4, 40.7
Tremolite	$Ca_2Mg_5(Si_8O_{22})(OH)_2$	10.5

Data availability

Data will be made available on request.

References

[1] P.J.M. Monteiro, S.A. Miller, A. Horvath, Towards sustainable concrete, Nat. Mater. 16 (7) (2017) 698–699.
[2] M. Hou, Z. Li, V.C. Li, Green and durable engineered cementitious composites (GD-ECC) with recycled PE fiber, desert sand, and carbonation curing: mixture design, durability performance, and life-cycle analysis, Constr. Build. Mater. 414 (2024) 134984.
[3] A.P. Gursel, E. Masanet, A. Horvath, A. Stadel, Life-cycle inventory analysis of concrete production: a critical review, Cem. Concr. Compos 51 (2014) 38–48.
[4] I.H. Shah, S.A. Miller, D. Jiang, R.J. Myers, Cement substitution with secondary materials can reduce annual global CO2 emissions by up to 1.3 gigatons, Nat. Commun. 13 (1) (2022) 5758.
[5] G. Habert, Y. Bouzidi, C. Chen, A. Jullien, Development of a depletion indicator for natural resources used in concrete, Resour. Conserv. Recycl 54 (6) (2010) 364–376.
[6] P. Peduzzi, Sand, rarer than one thinks, Environ. Dev. 11 (208–218) (2014) 682.
[7] Y. Liu, H. Huang, Z. Qiu, J. Fan, Detecting coastline change from satellite images based on beach slope estimation in a tidal flat, Int. J. Appl. Earth Obs. Geoinf. 23 (2013) 165–176.
[8] M.G.M. Elipe, S. López-Querol, Aeolian sands: characterization, options of improvement and possible employment in construction–The State-of-the-art, Constr. Build. Mater. 73 (2014) 728–739.
[9] H. Tsoar, The ecological background, deterioration and reclamation of desert dune sand, Agric. Ecosyst. Environ. 33 (2) (1990) 147–170.
[10] I. Livingstone, G.F.S. Wiggs, C.M. Weaver, Geomorphology of desert sand dunes: a review of recent progress, Earth-Sci. Rev. 80 (3–4) (2007) 239–257.
[11] R. Deng, X. Shen, Q. Liu, L. Wei, C. Zhang, Influence mechanism of pore characteristics of aeolian sand concrete on its strength, Bull. Chin. Ceram. Soc. 38 (2019) 1901–1907.
[12] F.J. Luo, L. He, Z. Pan, W.H. Duan, X.L. Zhao, F. Collins, Effect of very fine particles on workability and strength of concrete made with dune sand, Constr. Build. Mater. 47 (2013) 131–137.

[13] B.M. Das, N. Sivakugan, Principles of foundation engineering, Cengage learning, 2018.

[14] M.I. El-Sayed, Sedimentological characteristics and morphology of the aeolian sand dunes in the eastern part of the UAE, a case study from Ar Rub'Al Khali, Sediment. Geol. 123 (3–4) (1999) 219–238.

[15] E. Seif, E.S. Sedek, Performance of cement mortar made with fine aggregates of dune sand, Kharga Oasis, Western Desert, Egypt: an experimental study, Jordan J. Civ. Eng. 7 (3) (2013) 270–284.

[16] E.-S.S. Abu Seif, A.R. Sonbul, B.A.H. Hakami, E.K. El-Sawy, Experimental study on the utilization of dune sands as a construction material in the area between Jeddah and Mecca, Western Saudi Arabia, Bull. Eng. Geol. Environ. 75 (2016) 1007–1022.

[17] J. Kaufmann, Evaluation of the combination of desert sand and calcium sulfoaluminate cement for the production of concrete, Constr. Build. Mater. 243 (2020) 118281.

[18] J. Jiang, et al., Quasi-static and dynamic mechanical properties of eco-friendly ultra-high-performance concrete containing aeolian sand, Cem. Concr. Compos 97 (2019) 369–378.

[19] K.L. Scrivener, R.J. Kirkpatrick, Innovation in use and research on cementitious material, Cem. Concr. Res. 38 (2) (2008) 128–136.

[20] E. Fehling, M. Schmidt, J. Walraven, T. Leutbecher, S. Fröhlich, Ernst Sohn Berlin, Ger, Ultra-High. Perform. Concr. UHPC (2014) 25–32.

[21] J. Du, et al., New development of ultra-high-performance concrete (UHPC), Compos. Part B Eng. 224 (2021) 109220.

[22] M. Amran, S.-S. Huang, A.M. Onaizi, N. Makul, H.S. Abdelgader, T. Ozbakkaloglu, Recent trends in ultra-high performance concrete (UHPC): current status, challenges, and future prospects, Constr. Build. Mater. 352 (2022) 129029.

[23] Y. Shi, G. Long, C. Ma, Y. Xie, J. He, Design and preparation of ultra-high performance concrete with low environmental impact, J. Clean. Prod. 214 (2019) 633–643.

[24] S. Abbas, M.L. Nehdi, M.A. Saleem, Ultra-high performance concrete: mechanical performance, durability, sustainability and implementation challenges, Int. J. Concr. Struct. Mater. 10 (2016) 271–295.

[25] M.C.G. Juenger, F. Winnefeld, J.L. Provis, J.H. Ideker, Advances in alternative cementitious binders, Cem. Concr. Res. 41 (12) (2011) 1232–1243, https://doi.org/10.1016/j.cemconres.2010.11.012.

[26] D.-Y. Yoo, N. Banthia, I. You, S.-J. Lee, Recent advances in cementless ultra-high-performance concrete using alkali-activated materials and industrial byproducts: a review, Cem. Concr. Compos (2024) 105470.

[27] D. Wang, C. Shi, Z. Wu, J. Xiao, Z. Huang, Z. Fang, A review on ultra high performance concrete: part II. Hydration, microstructure and properties, Constr. Build. Mater. 96 (2015) 368–377.

[28] Y. Ma, et al., Heating-induced transformations in calcium silicate hydrate (C-S-H): In-situ investigations of composition, structure, and morphology, Cem. Concr. Res. 190 (2025) 107819, https://doi.org/10.1016/j.cemconres.2025.107819.

[29] X. Wang, J. Zhong, Y. Sun, Innovative strategy to reduce autogenous shrinkage in alkali-activated slag using hydrophilic carbon nanotube sponge, Compos. Part B Eng. (2025) 112447.

[30] D. Xia, R. Chen, J. Cheng, Y. Tang, C. Xiao, Z. Li, Desert sand-high calcium fly ash-based alkali-activated mortar: flowability, mechanical properties, and microscopic analysis, Constr. Build. Mater. 398 (2023) 131729.

[31] D. Yang, et al., Effects of red mud, desert sand, and ground granulated blast furnace slag on the mechanical properties and microstructure of fly ash-based geopolymer, Constr. Build. Mater. 468 (2025) 140471, https://doi.org/10.1016/j.conbuildmat.2025.140471.

[32] Y. Liu, Z. Zhang, C. Shi, D. Zhu, N. Li, Y. Deng, Development of ultra-high performance geopolymer concrete (UHPGC): influence of steel fiber on mechanical properties, Cem. Concr. Compos 112 (2020) 103670.

[33] Y. Zuo, M. Nedeljković, G. Ye, Pore solution composition of alkali-activated slag/fly ash pastes, Cem. Concr. Res. 115 (2019) 230–250, https://doi.org/10.1016/j.cemconres.2018.10.010.

[34] Y. Sun, M.K. Mohan, X. Dai, Y. Zhang, G. Ye, G.De Schutter, Effects of mixing conditions and activator anionic species on the rheology of silicate-activated slag concrete, Cem. Concr. Compos 150 (2024) 105556.

[35] Y. Sun, et al., Cement and concrete research interpretation of the early stiffening process in alkali-activated slag pastes, no. November 2022, Cem. Concr. Res 167 (2023) 107118, https://doi.org/10.1016/j.cemconres.2023.107118.

[36] Y. Sun, et al., A conceptual design of two-stream alkali-activated materials, Cem. Concr. Compos 148 (2024) 105485, https://doi.org/10.1016/j.cemconcomp.2024.105485.

[37] Y. Sun, Z. Liu, S. Ghorbani, G. Ye, G. De Schutter, Fresh and hardened properties of alkali-activated slag concrete: The effect of fly ash as a supplementary precursor (no. March), J. Clean. Prod. 370 (2022) 133362, https://doi.org/10.1016/j.jclepro.2022.133362.

[38] W. Tu, G. Fang, B. Dong, M. Zhang, Micromechanical analysis of alkali-activated fly ash-slag paste subjected to elevated temperatures, Cem. Concr. Compos (2024) 105735.

[39] G. Fang, M. Zhang, Multiscale micromechanical analysis of alkali-activated fly ash-slag paste, Cem. Concr. Res. 135 (2020) 106141.

[40] W.C. Oliver, G.M. Pharr, An improved technique for determining hardness and elastic modulus using load and displacement sensing indentation experiments, J. Mater. Res. 7 (6) (1992) 1564–1583.

[41] C. Hu, D. Hou, Z. Li, Micro-mechanical properties of calcium sulfoaluminate cement and the correlation with microstructures, Cem. Concr. Compos 80 (2017) 10–16.

[42] Z. Jia, C. Chen, H. Zhou, Y. Zhang, The characteristics and formation mechanism of the dark rim in alkali-activated slag, Cem. Concr. Compos 112 (2020) 103682.

[43] R.M. Arachchige, J. Olek, F. Rajabipour, S. Peethamparan, Phase identification and micromechanical properties of non-traditional and natural pozzolan based alkali-activated materials, Constr. Build. Mater. 441 (2024) 137478.

[44] Z. Luo, W. Li, K. Wang, A. Castel, S.P. Shah, Comparison on the properties of ITZs in fly ash-based geopolymer and Portland cement concretes with equivalent flowability, Cem. Concr. Res. 143 (2021) 106392.

[45] P. Duxson, J.L. Provis, Designing precursors for geopolymer cements, J. Am. Ceram. Soc. 91 (12) (2008) 3864–3869, https://doi.org/10.1111/j.1551-2916.2008.02787.x.

[46] Y. Sun, B. Chen, S. Zhang, K. Blom, M. Luković, G. Ye, Characterization, pre-treatment, and potential applications of fine MSWI bottom ash as a supplementary cementitious material, Constr. Build. Mater. 421 (2024) 135769, https://doi.org/10.1016/j.conbuildmat.2024.135769.

[47] Z. Shi, Green manufacturing of silicate materials using desert sand as a raw-material resource, Constr. Build. Mater. 338 (2022) 127539.

[48] M. Zhang, X. Zhu, J. Shi, B. Liu, Z. He, C. Liang, Utilization of desert sand in the production of sustainable cement-based materials: A critical review, Constr. Build. Mater. 327 (2022) 127014.

[49] X. Dai, S. Aydin, M.Y. Yardimci, K. Lesage, G.De Schutter, Early age reaction, rheological properties and pore solution chemistry of NaOH-activated slag mixtures, Cem. Concr. Compos 133 (2022) 104715.

[50] A.R. Santos, M. do R. Veiga, A. Santos Silva, J. de Brito, J.I. Álvarez, Evolution of the microstructure of lime based mortars and influence on the mechanical behaviour: the role of the aggregates, Constr. Build. Mater. 187 (2018) 907–922, https://doi.org/10.1016/j.conbuildmat.2018.07.223.

[51] J. Yang, et al., The influence of graphene oxide on the hydration and mechanical properties of cement-based materials with low water-binder ratio, Cem. Concr. Compos 152 (2024) 105640, https://doi.org/10.1016/j.cemconcomp.2024.105640.

[52] K.L. Scrivener, A.K. Crumbie, P. Laugesen, The interfacial transition zone (ITZ) between cement paste and aggregate in concrete, Interface Sci. 12 (4) (2004) 411–421, https://doi.org/10.1023/B:INTS.0000042339.92990.4c.

[53] K.-Y. Liao, P.-K. Chang, Y.-N. Peng, C.-C. Yang, A study on characteristics of interfacial transition zone in concrete, Cem. Concr. Res. 34 (6) (2004) 977–989.

[54] Y. Sun, S. Ghorbani, X. Dai, G. Ye, G.De Schutter, Evaluation of rheology and strength development of alkali-activated slag with different silicates sources, Cem. Concr. Compos (2022) 104415.

[55] F. Puertas, A. Fernández-Jiménez, M.T. Blanco-Varela, Pore solution in alkali-activated slag cement pastes. Relation to the composition and structure of calcium silicate hydrate, Cem. Concr. Res. 34 (1) (Jan. 2004) 139–148, https://doi.org/10.1016/S0008-8846(03)00254-0.

[56] S.A. Bernal, R.M. de Gutierrez, J.L. Provis, V. Rose, Effect of silicate modulus and metakaolin incorporation on the carbonation of alkali silicate-activated slags, Cem. Concr. Res. 40 (6) (2010) 898–907, https://doi.org/10.1016/j.cemconres.2010.02.003.

[57] Z. Zhang, Y. Zhu, H. Zhu, Y. Zhang, J.L. Provis, H. Wang, Effect of drying procedures on pore structure and phase evolution of alkali-activated cements, no. November 2018, Cem. Concr. Compos 96 (2019) 194–203, https://doi.org/10.1016/j.cemconcomp.2018.12.003.

[58] S. Ghorbani, et al., Characterisation of alkali-activated stainless steel slag and blast-furnace slag cements, Cem. Concr. Compos 143 (2023) 105230.

[59] A.R. Brough, A. Atkinson, Sodium silicate-based, alkali-activated slag mortars: Part I. Strength, hydration and microstructure, Cem. Concr. Res. 32 (6) (2002) 865–879.

[60] F. Puertas, M. Palacios, H. Manzano, J.S. Dolado, A. Rico, J. Rodríguez, A model for the C-A-S-H gel formed in alkali-activated slag cements, J. Eur. Ceram. Soc. 31 (12) (2011) 2043–2056, https://doi.org/10.1016/j.jeurceramsoc.2011.04.036.

[61] W. Kunther, S. Ferreiro, J. Skibsted, Influence of the Ca/Si ratio on the compressive strength of cementitious calcium–silicate–hydrate binders, J. Mater. Chem. A 5 (33) (2017) 17401–17412.

[62] Y. Li, H. Zhang, G. Liu, D. Hu, X. Ma, Multi-scale study on mechanical property and strength prediction of aeolian sand concrete, Constr. Build. Mater. 247 (2020) 118538.

[63] G. Fang, Q. Wang, M. Zhang, Micromechanical analysis of interfacial transition zone in alkali-activated fly ash-slag concrete, Cem. Concr. Compos 119 (2021) 103990.

[64] K. Wu, H. Shi, L. Xu, G. Ye, G. De Schutter, Microstructural characterization of ITZ in blended cement concretes and its relation to transport properties, Cem. Concr. Res. 79 (2016) 243–256, https://doi.org/10.1016/j.cemconres.2015.09.018.

[65] C. Li, J. Zhong, Y. Sun, Novel approach to enhance the damping performance of cement-based materials through polymer/carbon nanotube composite coating and gradation of aggregates, Constr. Build. Mater. 471 (2025) 140708.

[66] G. Habert, C. Ouellet-Plamondon, Recent update on the environmental impact of geopolymers, RILEM Tech. Lett. 1 (2016) 17–23.

[67] J. Yu, et al., Tensile performance of sustainable strain-hardening cementitious composites with hybrid PVA and recycled PET fibers, Cem. Concr. Res. 107 (2018) 110–123.

[68] D. Wang, J. Che, C. Liu, H. Liu, Design of mixture proportion of engineered cementitious composites based on desert sand, KSCE J. Civ. Eng. (2024) 1–11.

[69] J. Du, Z. Liu, C. Christodoulatos, M. Conway, Y. Bao, W. Meng, Utilization of off-specification fly ash in preparing ultra-high-performance concrete (UHPC): mixture design, characterization, and life-cycle assessment, Resour. Conserv. Recycl 180 (2022) 106136.

[70] G. Liang, L. Luo, W. Yao, Reusing waste red brick powder as partial mineral precursor in eco-friendly binders: reaction kinetics, microstructure and life-cycle assessment, Resour. Conserv. Recycl 185 (2022) 106523.

[71] K. Khan, M.A.M. Johari, M.N. Amin, M. Iqbal, Evaluation of the mechanical properties, microstructure, and environmental impact of mortar incorporating metakaolin, micro and nano-silica, Case Stud. Constr. Mater. 20 (2024) e02699, https://doi.org/10.1016/j.cscm.2023.e02699.

[72] P.S.M. Thilakarathna, S. Seo, K.S.K. Baduge, H. Lee, P. Mendis, G. Foliente, Embodied carbon analysis and benchmarking emissions of high and ultra-high strength concrete using machine learning algorithms, J. Clean. Prod. 262 (2020) 121281, https://doi.org/10.1016/j.jclepro.2020.121281.

[73] N.P. Rajamane, M.C. Nataraja, N. Lakshmanan, J.K. Dattatreya, and D. Sabitha, Sulphuric acid resistant ecofriendly concrete from geopolymerisation of blast furnace slag, 2012.

[74] H.S. Müller, M. Haist, M. Vogel, Assessment of the sustainability potential of concrete and concrete structures considering their environmental impact, performance and lifetime, Constr. Build. Mater. 67 (2014) 321–337.

[75] P. Kathirvel, S. Sreekumaran, Sustainable development of ultra high performance concrete using geopolymer technology, J. Build. Eng. 39 (2021) 102267.

[76] X. Gao, X. Yao, T. Yang, S. Zhou, H. Wei, Z. Zhang, Calcium carbide residue as auxiliary activator for one-part sodium carbonate-activated slag cements: compressive strength, phase assemblage and environmental benefits, Constr. Build. Mater. 308 (2021) 125015, https://doi.org/10.1016/j.conbuildmat.2021.125015.

[77] X. Gao, X. Yao, T. Yang, S. Zhou, H. Wei, Z. Zhang, Calcium carbide residue as auxiliary activator for one-part sodium carbonate-activated slag cements: compressive strength, phase assemblage and environmental benefits, Constr. Build. Mater. 308 (2021) 125015, https://doi.org/10.1016/j.conbuildmat.2021.125015.

[78] G.W. Kim, et al., Hybrid reinforcement of steel–polyethylene fibers in cementless ultra-high performance alkali-activated concrete with various silica sand dosages, Constr. Build. Mater. 394 (2023) 132213.

[79] Y.I.A. Aisheh, D.S. Atrushi, M.H. Akeed, S. Qaidi, B.A. Tayeh, Influence of steel fibers and microsilica on the mechanical properties of ultra-high-performance geopolymer concrete (UHP-GPC), Case Stud. Constr. Mater. 17 (2022) e01245.

[80] Y. Liu, C. Shi, Z. Zhang, N. Li, D. Shi, Mechanical and fracture properties of ultra-high performance geopolymer concrete: effects of steel fiber and silica fume, Cem. Concr. Compos 112 (2020) 103665.

[81] S.H.G. Mousavinejad, M. Sammak, An assessment of the effect of Na2SiO3/NaOH ratio, NaOH solution concentration, and aging on the fracture properties of ultra-high-performance geopolymer concrete: The application of the work of fracture and size effect methods. Structures, Elsevier, 2022, pp. 434–443.

[82] S. Xu, et al., Development and preliminary mix design of ultra-high-performance concrete based on geopolymer, Constr. Build. Mater. 308 (2021) 125110.

[83] S.H.G. Mousavinejad, M. Sammak, Strength and chloride ion penetration resistance of ultra-high-performance fiber reinforced geopolymer concrete. Structures, Elsevier, 2021, pp. 1420–1427.

[84] G.W. Kim, T. Oh, S.K. Lee, N. Banthia, D.-Y. Yoo, Development of Ca-rich slag-based ultra-high-performance fiber-reinforced geopolymer concrete (UHP-FRGC): Effect of sand-to-binder ratio, Constr. Build. Mater. 370 (2023) 130630.

[85] R. Zhang, H. He, Y. Song, X. Zhi, F. Fan, Influence of mix proportioning parameters and curing regimes on the properties of ultra-high strength alkali-activated concrete, Constr. Build. Mater. 393 (2023) 132139.